Journal of Magnetism and Magnetic Materials 407 (2016) 299–307

Contents lists available at ScienceDirect

Journal of Magnetism and Magnetic Materials

journal homepage: www.elsevier.com/locate/jmmm

Magnetic behavior of iron-modified MCM-41 correlated with clustering processes from the wet impregnation method

Natalia I. Cuello [a], Verónica R. Elías [a], Elin Winkler [b], Gabriela Pozo-López [c], Marcos I. Oliva [c], Griselda A. Eimer [a,*]

[a] Centro de Investigación y Tecnología Química (CITeQ) (UTN-CONICET), Facultad Regional Córdoba. Maestro López y Cruz Roja Argentina, Ciudad Universitaria, Córdoba 5016, Argentina
[b] Centro Atómico Bariloche, Comisión Nacional de Energía Atómica – CONICET, Avenue Bustillo 9500, San Carlos de Bariloche 8400, Argentina
[c] Facultad de Matemática, Astronomía y Física, Universidad Nacional de Córdoba – IFEG, CONICET, Ciudad Universitaria, Córdoba 5000, Argentina

ARTICLE INFO

Article history:
Received 18 September 2015
Received in revised form
11 December 2015
Accepted 1 January 2016
Available online 3 February 2016

Keywords:
Fe-modified MCM-41
Wet impregnation
Superparamagnetism
ZFC–FC curves
Blocking temperature

ABSTRACT

Magnetic MCM-41 type mesoporous silica materials were synthetized and modified with different iron loadings by the wet impregnation method. The evolution of iron speciation, depending on the metal loading and associated with a particular magnetic behavior was investigated by *M vs. H* curves, FC–ZFC curves, EPR spectroscopy and other complementary techniques such as SEM, TEM, and chemisorption of pyridine followed by FT-IR studies. A superparamagnetic contribution was larger for the lower loadings suggesting the high dispersion of very small sized iron nanospecies. However, this contribution decreased with increasing metal loading due to the growth of magnetically blocked nanoparticles (hematite) on the outer surface. Finally, a bimodal size distribution for the superparamagnetic nanospecies could be inferred; then the anisotropy constant for this phase and the corresponding nanospecies sizes were estimated.

1. Introduction

During the last decade, iron oxide nanospecies have been the focus of research interest due to a wide variety of properties. These properties give them a huge potential for their application as magnetic resonance imaging agents, heat mediators in cancer treatment by hyperthermia, solid support in heterogeneous catalysis, biosensors, adsorbents for the removal of dyes and metals, and as magnetic guides in drug delivery systems, through a technique known as magnetic targeting [1–4].

However, nanosized magnetic particles are extremely difficult to synthesize because they tend to aggregate and/or coalesce. In response to this problem, the synthesis of nanoparticles into porous solid supports appears as very promising. Thus, magnetic particle agglomeration may be completely inhibited and the stability of small sized metal and metal oxide nanoparticles enhanced [5,6]. Particularly, MCM-41 is one of the most attractive porous materials because of its characteristic well-ordered structure with a hexagonal arrangement of mesopores and large specific area ($>900\ m^2/g$) [7,8]. This available surface could lead to higher loading capacity of guest molecules that, besides the thermal stability and biocompatibility, has made them highly interesting for multiple applications [9–14].

The size dependence of the magnetic properties of nanoparticles has attracted much attention from both a theoretical and an experimental point of view [1,2]. The properties of magnetic nanoparticles can differ considerably from those of bulk materials. In large magnetic particles, it is well known that there is a multidomain structure, where regions of uniform magnetization are separated by domain walls. If the sample size is reduced, there is a critical volume below which it takes more energy to create a domain wall than to support the external magnetostatic energy (stray field) of the single-domain state. This critical diameter, below which a superparamagnetic behavior can be observed, typically lies in the range of a few tens of nanometers depending on the material. On the other hand, the dynamics of the relaxation behavior of superparamagnetic nanoparticles is mainly governed by the anisotropy energy [15]. The magnetization vector in a single-domain particle tends to align along one direction, called the easy axis, which results in minimum anisotropy energy. This anisotropy energy acts as an energy barrier that limits the free rotation of the magnetic moments away from the easy axis. When the energy barrier is overcome thermally, magnetization can reverse its direction rapidly, exhibiting a superparamagnetic relaxation. For noninteracting particles with uniaxial anisotropy, the

* Corresponding author. Tel./fax: +543514690585.
E-mail addresses: geimer@frc.utn.edu.ar, griseeimer@yahoo.com.ar (G.A. Eimer).

http://dx.doi.org/10.1016/j.jmmm.2016.01.004
0304-8853/

relaxation time for the reversal process is described by the Néel–Arrhenius equation [16]. Since the magnetic anisotropy constant determines the energy barrier for the coherent rotation of the particle moment, and therefore affects the shape of hysteresis loops controlling the coercivity and remanence, its characterization is very important for practical applications. In this sense, it is known that the magnetic anisotropy constant increases strongly with decreasing particle size [17].

Although some analyses about the behavior of magnetic nanoparticles formed on mesoporous materials have been reported, they are scarce and shallow [18–21]. Here, we propose a thorough study of the magnetic behavior of iron-modified mesoporous materials in relation to the evolution of the nanospecies formed and their size distribution as a function of increasing metal loading. In addition, the influence of temperature on magnetization and the determination of the anisotropy constant for the superparamagnetic phase allowed us to have a better knowledge of process clustering resulting from this method of synthesis.

2. Experimental

2.1. Synthesis

The MCM-41 type mesoporous molecular sieve was synthesized as previously reported [22], using cetyltrimethylammonium bromide (CTAB) as template and tetraethoxysilane (TEOS) as silicon source. The synthesis mixture (pH = 11.25) was stirred at room temperature for 4 h. Then, this gel was heated at 340 K under stirring in a closed flask. The obtained solid was then filtered off, washed with distilled water, and dried at 333 K overnight. The template was evacuated from the samples by heating (2 K/min) under N_2 flow (45 mL/min) at 773 K for 6 h and then calcined at 773 K for 6 h under dry air flow (45 mL/min). This solid, previously calcined for 5 h in an oven at 773 K, was modified with iron by the wet impregnation method. Different concentrations of an aqueous solution of the metal precursor $Fe(NO_3)_3 \cdot 9H_2O$ were used to reach the desired metal loadings, (0.0036; 0.009; 0.018; 0.039; 0.062 M corresponding to 15, 10, 5, 2.5 and 1 wt%, respectively). The MCM-41 host was dispersed in the precursor solution at room temperature and then, the solvent (water) was slowly removed by rotary evaporation at 330 K for 30 min. The resulting powder was dried at 330 K and calcined at 773 K for 9 h. Samples were designated as Fe/M(x), where M indicates the MCM-41 mesoporous structure and x indicates the nominal metal loading in wt%.

2.2. Characterization

X-ray diffraction patterns (XRD) were recorded in a Philips PW 3830 diffractometer with Cu Kα radiation ($\lambda = 1.5418$ Å) in the range of 2θ from 1.5° to 7° and from 20° to 80°. SEM micrographs were obtained in a JEOL model JSM 6380 LV. Gold coverage was applied to make samples conductive. The acceleration voltage was 20 kV. Transmission electron microscopy (TEM) observations and selected area diffraction patterns were performed in a Philips CM200UT microscope, operating at 200 kV and equipped with energy-dispersive X-ray spectroscopy (EDS) facility. Samples were prepared by dispersing a small amount of powder in ethanol and depositing a drop of this emulsion on a holey carbon-coated copper grid. The specific surface, the pore size distribution, and the total pore volume were calculated from N_2 adsorption–desorption isotherms obtained at 77 K using a Micromeritics ASAP 2010. The surface was determined by the Brunauer–Emmett–Teller (BET) method in the pressure range of P/P_0: 0.01–0.21, and the pore size by the NLDFT method. The Fe content was calculated by inductively coupled plasma optical emission spectroscopy (ICP) using a VISTA–MPX CCD Simultaneous ICP-OES-VARIAN. XPS analysis were performed on a computer equipped with a Multitechnique Specs Dual X-ray source Mg/Al model XR50 and hemispherical energy analyzer 150 PHOIBOS operated in FAT (fixed analyzer transmission. Spectra were obtained with a power passage 30 eV and Al anode operated at 100 and 150 W when the conditions in the main chamber were adequate. The pressure during the measurement was less than 2×10^{-8} mbar. Samples were supported on double-sided Cu tape and then subjected to ultrahigh vacuum evacuation for 12 h prior to the readings. FT-IR spectral measurements of pyridine adsorption on the samples were performed on a JASCO FT-IR 5300 spectrometer equipped with a DTGS detector. The range and resolution of acquisition data were 4600–400 and 4 cm^{-1}, respectively. A self-supporting wafer for each sample (~20 mg and 13 mm of diameter) was prepared, placed in a thermostated cell with CaF_2 windows connected to a vacuum line, and evacuated at 673 K for 8 h. The background spectrum was recorded first after cooling the sample to room temperature. Afterwards, the solid wafer was exposed to pyridine vapors (Sintorgan, 99% purity) until the system was saturated to ~46 mm Hg at room temperature; the contact time at this pressure was 12 h. The FT-IR spectrum for each sample was obtained after pyridine desorption by evacuation at 473 or 573 K for 1 h. All the spectra were recorded at room temperature before and after pyridine adsorption and desorption at each temperature. Room temperature magnetization curves were measured in a vibrating sample magnetometer (VSM) LakeShore 7300, with static field up to $\mu_0 H = 1$ T. Magnetization *vs.* temperature curves were measured in a Quantum Design SQUID magnetometer up to 6 T. The hysteresis properties such as coercivity and remanence were obtained directly from the magnetization curves; these hysteresis curves were well fitted by the sum of three contributions: a linear paramagnetic or diamagnetic contribution (LM), a ferromagnetic one (FM), and a superparamagnetic-like one (SPM) [23], so that the total magnetization is: TM = LM + FM + SPM, with:

$$\mathrm{LM} = \chi \mu_0 H \tag{1}$$

$$\mathrm{FM} = \frac{2M_{SF}}{\pi}\left(\tan^{-1}\left(\frac{H + \mu_0 H_C}{\mu_0 H_C}\right)\tan\frac{\pi M_{RF}}{M_{SF}}\right) \tag{2}$$

$$\mathrm{SPM} = M_{SS}\left(\coth\frac{\mu_{SP} H}{K_B T} - \frac{K_B T}{\mu_{SP} H}\right) \tag{3}$$

where $\mu_0 H_C$, M_{SF}, and M_{RF} are the coercive field and the effective saturation and remanent magnetic moments, associated with the ferromagnetic contribution, respectively. M_{SS} is the effective saturation magnetic moment, and μ_{SP} is the mean magnetic moment of the superparamagnetic units [23]. The temperature dependence of the magnetization was measured following the conventional zero field cooling (ZFC) and field cooling (FC) protocols, under a small applied field of 10 mT.

3. Results and discussion

Fig. 1A shows the low-angle XRD patterns of the samples, which exhibit three diffraction peaks assignable to the hexagonal array of their unidimensional pores, characteristic of MCM-41 materials [22]. In this way, the mesoporous order is maintained after the Fe loading for all the metal contents. Other diffraction peaks can be observed, at around $2\theta = 33°$, 35° and 63°, for the highest loaded sample in its high-angle XRD pattern (Fig. 2B).

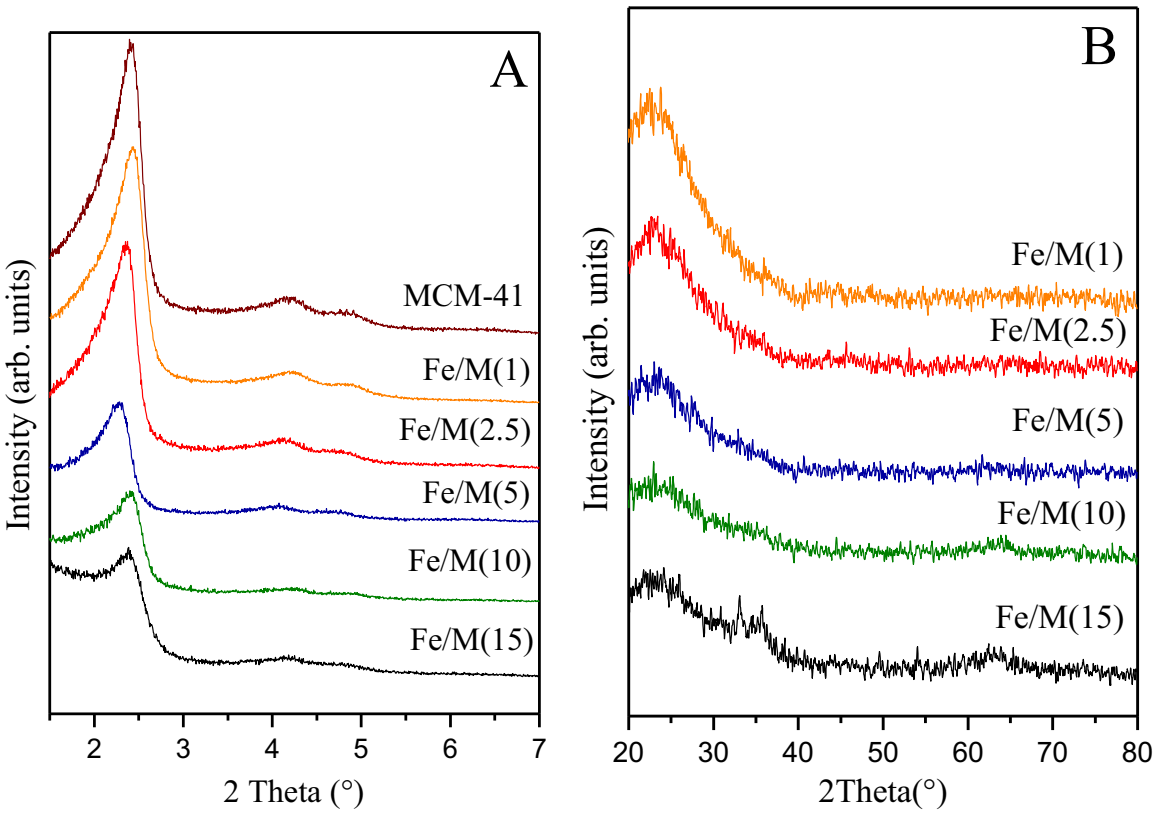

Fig. 1. (A) Low-angle XRD patterns and (B) high-angle XRD patterns of the synthesized samples.

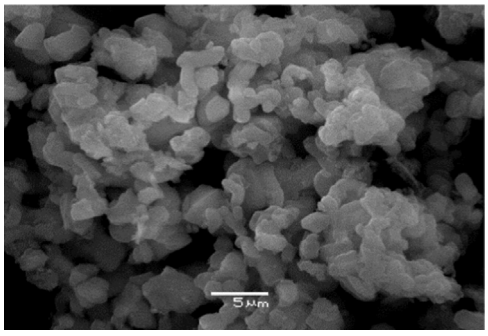

Fig. 2. Scanning electron microscopy image of Iron-modified MCM-41 (chosen as representative).

These peaks are related to some of the most intense diffraction lines of hematite (α-Fe_2O_3). An average crystallite size of about 25 nm was estimated for this phase, from the reflection lines (104) and (110) using the Scherrer equation [24,25]: $D=(0.9\lambda)/(\beta\cos\theta)$, where β (in radians) is the peak intrinsic breadth after subtraction of the instrumental contribution, λ is the X-ray wavelength and θ the diffraction (Bragg) angle. Peaks corresponding to Fe oxides do not appear in the XRD patterns for the lower Fe loaded samples, indicating that these species are amorphous or are clusters/particles too small to be detected by the XRD technique.

The particle size and morphology of Fe/M(x) samples were investigated by SEM. Fig. 2 shows a SEM image of an iron-modified sample chosen as representative. As it can be observed, the particles of the solid did not display any particular morphology. Anyway, particles with spherical-like morphology aggregated into

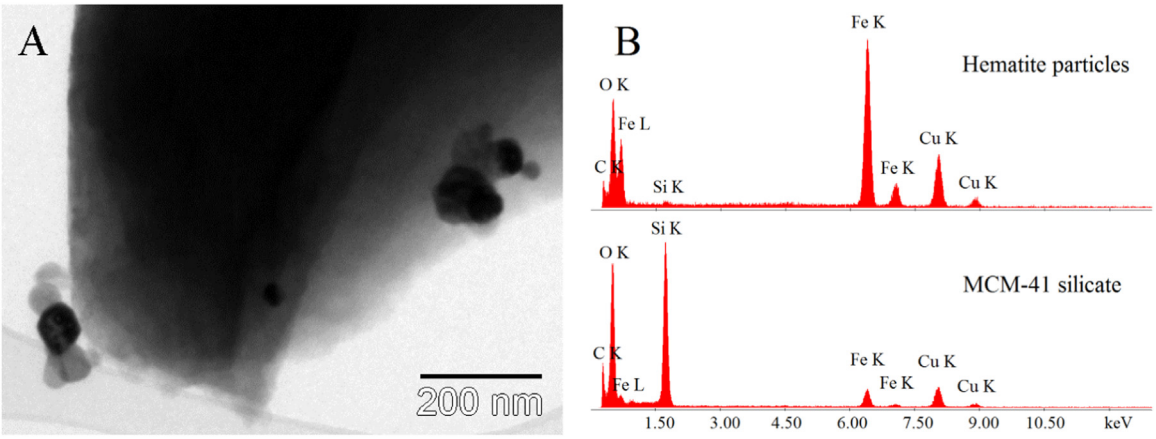

Fig. 3. (A) Bright field TEM image of sample Fe/M(15) showing hematite nanoparticles on the external surface of the silicate. (B) EDS spectra for the hematite particles and mesoporous silica. C and Cu lines arise from the grid.

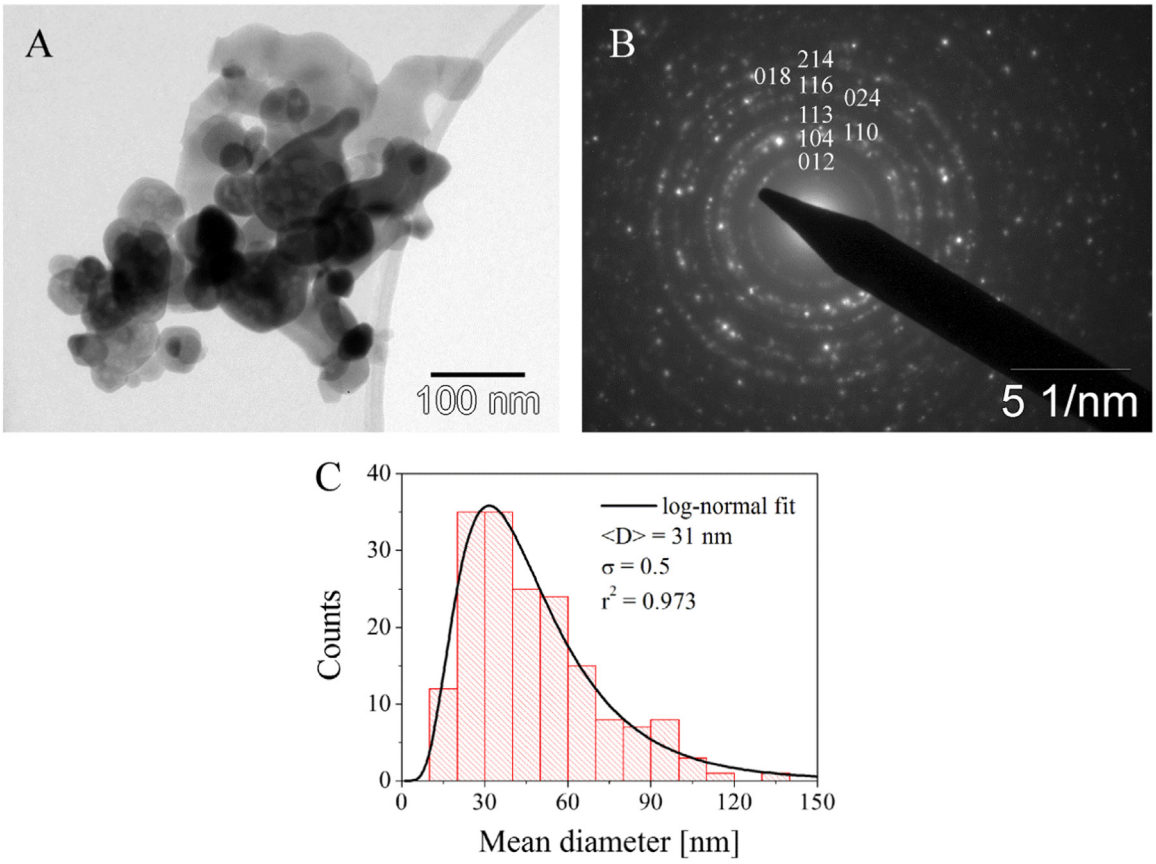

Fig. 4. (A) Bright field TEM image of an agglomerate of hematite particles grown outside the silicate in sample Fe/M(15). (B) Selected area diffraction pattern of an agglomerate showing the indexed diffraction rings from hematite phase. (C) Hematite particle size histogram, together with its corresponding log-normal distribution fitting.

larger secondary particles that occur in various morphologies and sizes could be observed.

In this study TEM was used to extend the structural analysis presented by us elsewhere [26] and corroborate the existence, morphology and sizes of the hematite nanoparticles detected in the Fe/M(15) sample by XRD. Thus, TEM images confirm the presence of crystalline hematite nanoparticles on the support external surface, arising from a clustering process favored by the high iron loading. Fig. 3 presents a bright field image of some hematite particles on the mesoporous silica surface and the corresponding EDS spectra for each phase. Fig. 4 shows an agglomerate of hematite particles (A) together with the corresponding selected area electron diffraction (SAED) pattern (B), in which the hematite indexed diffraction rings can be observed. The particle size histogram for hematite phase, determined from several TEM images, is presented in Fig. 4C. The histogram was fitted using a lognormal distribution of particle diameters, from which the mean particle diameter $<D>$ and the distribution width σ were obtained. The mean particle size obtained by TEM data ($<D>=31$ nm) agrees pretty well with the average crystallite size estimated from XRD measurements. With the aim of deepening about the role of the support structure in the nanocomposites, TEM images of the sample with lowest Fe loading, Fe/M(1), are shown in Fig. 5. In Fig. 5A_1 a frontal view of the arrangement of mesopores can be evidenced; meanwhile, Fig. 5A_2 mainly corresponds to views perpendicular to the direction of the pore arrangement and

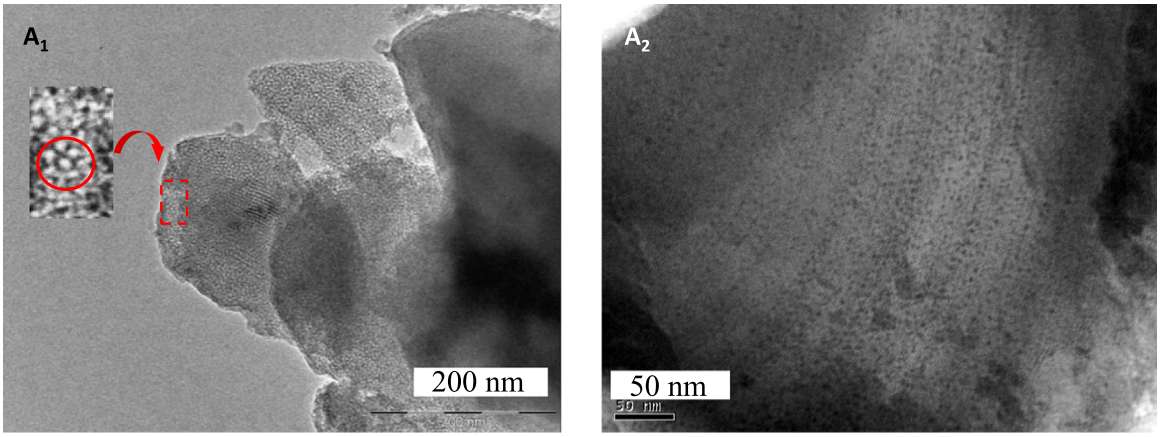

Fig. 5. Transmission electron microscopy images of Fe/M(1) sample.

unidirectional straight channels arranged along the long axis could be observed. The darker regions along the mesopores, seen in this last figure, are accounting for the incorporation of the Fe nanospecies inside the mesochannels. Thus, Fe nanospecies could be stabilized on the surface filling the pores as very small oxide clusters or nanoparticles. This fact would be evidencing the refiner effect carried out by the support structure, whose pore diameter limits the size of the iron nanospecies formed inside them. It can be seen that, unlike the Fe/M(15) sample, for this sample with low Fe-loading no large oxide particles are observed. Then, in the samples with low and high Fe-loadings, iron oxides nanospecies are formed within channels, but the growth of larger species on the external surface is enhanced by the increase in the metal loading. In this sense, the formation of the different Fe species in these materials can be explained taking account that after impregnation, Fe^{3+} ions can be stabilized on the surface by an anchoring reaction with oxygens of the structure until certain saturation coverage is reached. Beyond this limit, when the iron loading is increased, an incipient oligomerization of iron species containing Fe–O–Fe bonds starts to appear. Such clustering process would lead to the formation of very small oligonuclear $(FeO)_n$ clusters, and then, to the iron oxide nanoparticles of very small size. Finally, when the Fe-content is higher, the aggregation of the mentioned small clusters results in the formation of the bigger oxide particles observed on the external surface.

The chemisorption of pyridine followed by FT-IR studies, frequently used to detect Lewis and Brönsted acidic sites on solid catalysts [27–30], was employed by us here in order to complement the study on the nature of the different Fe species present in the samples. Fig. 6 shows the IR spectra following the chemisorption of pyridine after thermodesorption at 473 and 573 K, where the curves were affected by the pellet mass. It is known that pyridine is a basic molecule that can interact with acid sites via the nitrogen lone-pair electrons giving rise to different characteristic bands. Moreover the desorption at different temperatures can also give information about the strength of Lewis and Brönsted acid sites. In Fig. 6A, the curve corresponding to pure MCM-41obtained after desorption at 473 K shows two bands at 1597 and 1447 cm^{-1} corresponding to pyridine bonded to silanol groups (Py…H), whose hydroxyls are not capable of protonating pyridine. Meanwhile, the Fe-containing samples also show a band at 1610 cm^{-1} corresponding to an "electron-donor-acceptor" adduct between pyridine and Lewis acidic sites (Py…L) [27,28,31–35] which proportionally increases with the Fe loading. Furthermore, it can be observed that the band at 1597 cm^{-1} decreases for the two higher loaded samples, probably due to silanol blocking by the presence of oxide nanospecies. However, the band at 1447 cm^{-1} systematically increases with the growing Fe loading, accounting for the overlapping of both the hydrogen-bonded pyridine band (1447 cm^{-1}) and a band attributed to the Lewis-type adduct that frequently appears at 1450 cm^{-1} [36]. The origin of such Lewis acidity could arise from Fe unoccupied molecular orbitals present in both the isolated Fe species, linked to framework oxygen atoms in the channels, and the Fe oxide species. In addition, it should be noted that these Lewis acid sites were strong enough to retain the pyridine molecules up to 573 K. On the other hand, bands at 1540 and 1636 cm^{-1}, usually assigned to Brönsted acid sites, were observed for the higher loaded samples. According to other reports, it is possible to assume that the incorporation of Fe gives rise to the mentioned Brönsted acidic sites on the surface that are strong enough to protonate pyridine. This acidity can be attributed to the weakness of the strength of the SiO–H bonds due to the presence of Fe in the vicinity of the silanol groups, which would lead to some structural deformation and/or changes in the electron density around Si [37]. Nonetheless, these Brönsted acidic sites were weak judging by the disappearance of the corresponding peaks after evacuation at 573 K.

Fig. 7 shows the IR spectra in the hydroxyl range before pyridine adsorption followed by desorption at 673 K. For the pure MCM-41 and the lower iron loaded samples, an intense band at

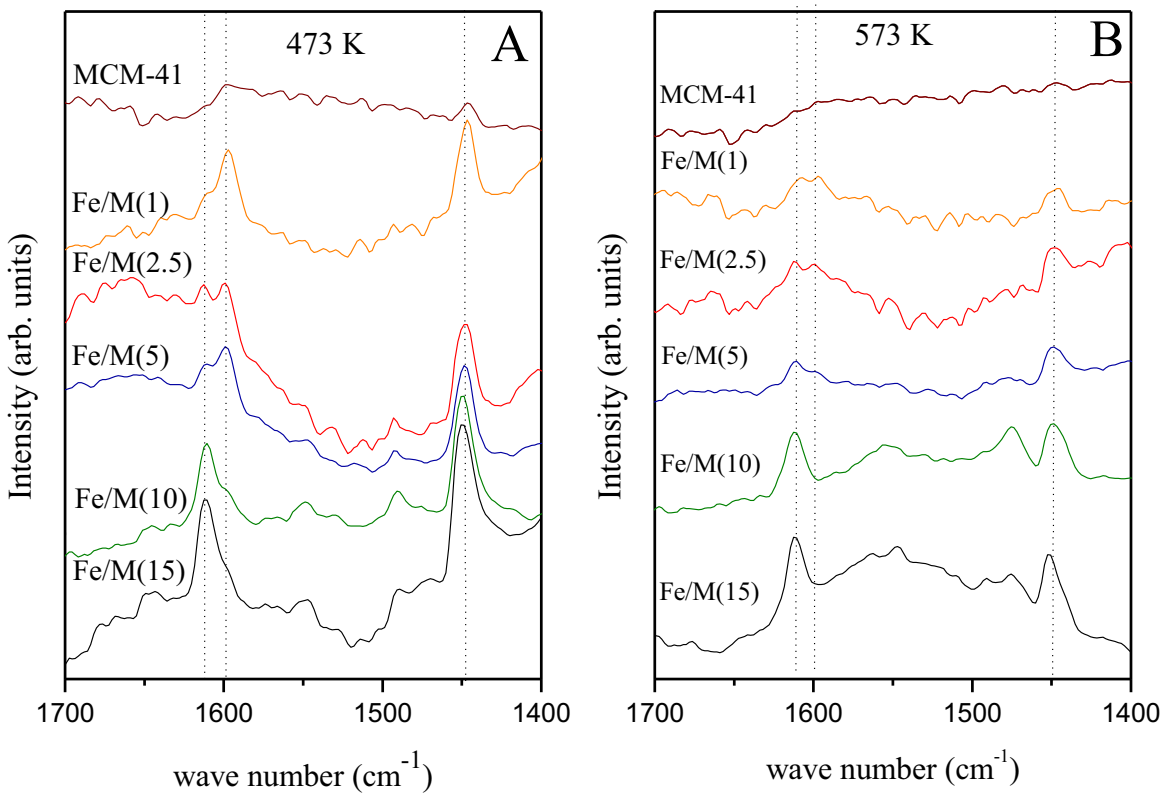

Fig. 6. FT-IR spectra of pyridine adsorbed on the samples Fe/M(x) and the bare MCM-41 material after evacuation at: (A) 473 K and (B) 573 K.

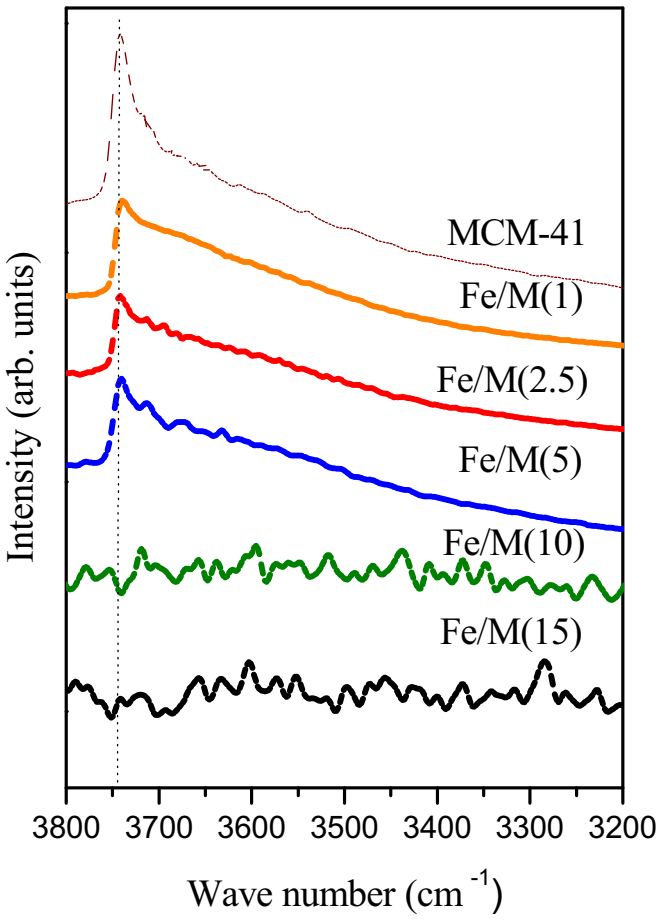

Fig. 7. FT-IR spectra in the hydroxyl stretching region after degassing at 673 K for all of the Fe/M(x) samples and the bare MCM-41 material.

3740 cm^{-1} corresponding to the stretching vibrations of isolated terminal hydroxyl groups was observed [38–43]. However, this band disappears for the higher loaded samples (Fe/M(10) and Fe/M(15)) likely due to an enhanced amount of oxide nanospecies that could be blocking the silanols, besides contributing to the Lewis acidity [44–45].

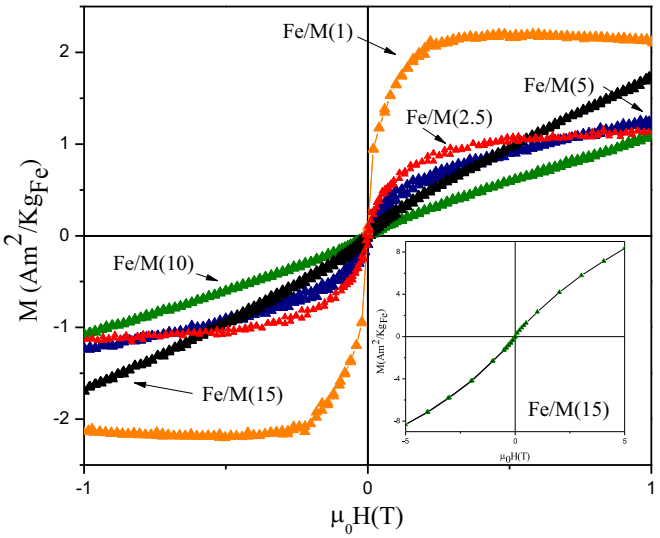

Fig. 8. Curves of magnetization versus applied field measured at room temperature for all Fe/M(x) samples studied in a VSM magnetometer. The inset box shows the measured Fe/M(15) sample cycle, also at 300 K in a SQUID magnetometer.

The magnetic moment curves as a function of applied field at room temperature for all samples are shown in Fig. 8. Given that Fe is the only possible source of magnetic signal, the units of magnetization are Am^2 per kilogram of Fe. As was reported by us elsewhere [26], a notable saturation magnetic moment appears for the lower loaded samples, assigned to a superparamagnetic contribution from the iron oxide species (clusters or nanoparticles) of very small size and finely dispersed on surface. This regime is detected in systems containing small, noninteracting single-domain particles. The single-domain critical size, above which particles develop domain walls and become multidomain, is an upper bound above which no superparamagnetism is observed. Thus, in the curves corresponding to the higher loaded samples (Fe/M(10) and Fe/M(15)) the notable attenuation of the superparamagnetic signal can arise from iron species magnetically blocked associated with the larger iron oxide nanoparticles grown up on the external surface [26]. Therefore, from a first observation of Fig. 8 it is possible to infer that the iron-modified materials show dia-, para-, superpara- and even ferromagnetic contributions. Here, in order to make a quantitative analysis, the magnetization curves were fitted using the Eqs. (1), (2) and (3) and the corresponding parameters are summarized in Table 1. It is noteworthy that for samples with nominal iron loading above 2.5 wt%, the sum of two contributions, a superparamagnetic and a ferromagnetic one, was required in the fit. Thus, the total magnetization is consistent with the presence of nanoclusters and nanoparticles in superparamagnetic regime (SPM) and larger hematite nanoparticles that would lead to the ferromagnetic contribution (FM). Hematite is an iron oxide with canted antiferromagnetic behavior at room temperature; as such, its magnetic contribution per unit volume is low, although the presence of edge effects causes decompensated spins. This fact would lead to the appearance of a small coercivity and magnetic remanence, which requires the addition of a ferromagnetic component in the total magnetization. Meanwhile, since the coercivity and remanence are negligible for the lower loaded samples, their curves could be fitted only with a superparamagnetic contribution. Moreover, it should be noted that, in the case of the Fe/M (1) sample, the presence of a negative linear diamagnetic contribution from the silica matrix is observed. Finally, the magnetic moment of the superparamagnetic units (μ_{SP}) decreasing with iron loading, observed in Table 1, could be indicating the growth in size of the particles on the external surface at the expense of superparamagnetic nanoclusters and/or nanoparticles of smaller size.

In order to continue with this analysis, the temperature dependence of the magnetization was performed. Fig. 9 shows the *zero-field-cooling* (ZFC) and *field-cooling* (FC) curves for Fe/M (1) and Fe/M(15) samples, measured with an applied field of 0.01 T. In both cases, a reversible behavior for temperatures above ~200 K can be observed. Below this temperature, the systems present an irreversible behavior with two anomalies in the ZFC curve, which could be associated with a bimodal distribution of blocking temperatures of the magnetic nanoparticles. Blocking temperature (T_B) is the characteristic temperature that separates the superparamagnetic regime from a blocked one and depends on the measurement time. This temperature is also associated with the energy barrier between the magnetic regimens, and therefore increases with increasing particle size. Thus, from ZFC and FC magnetization curves, it is possible to estimate the distribution of the energy barrier of the samples, according to [46]:

$$f(T_B) \propto \cdot d(M_{ZFC} - M_{FC})/dT \quad (4)$$

From Eq. (4) the median of the blocking temperature, $\langle T_B \rangle$, can be calculated by fitting $f(T_B)$ with a lognormal function. The inset in Fig. 9 shows the energy barrier distribution for Fe/M(1) and Fe/M(15)samples, from which $\langle T_B \rangle$~79 K and ~70 K are obtained,

Table 1
Magnetic parameters after fitting to data of Fig. 5.

Sample names	Fe Content (wt%)[a]	M_{SF} [$\frac{mAm^2}{Kg_{Fe}}$]	M_{RF} [$\frac{mAm^2}{Kg_{Fe}}$]	$\mu_0 H_C$ [T]	M_{SS} [$\frac{Am^2}{Kg_{Fe}}$]	μ_{SP} [μ_B]	$\mu_0\chi$ [$\frac{Am^2}{T.Kg_{Fe}}$]
Fe/M(1)	0.92	–	–	–	2.44	15017	−0.27
Fe/M(2.5)	2.56	–	–	–	1.15	8408	–
Fe/M(5)	4.24	547	11	17	1.46	725	–
Fe/M(10)	8.33	129	16	12	28.54	41.74	–
Fe/M(15)	12.55	415	54	55	87.89	27.49	–

M_{SF}: ferromagnetic effective saturation moment, M_{RF}: remanent moment, $\mu_0 H_C$: coercivity field, M_{SS}: superparamagnetic effective saturation moment μ_{SP}: magnetic moment of the superparamagnetic units, and $\mu_0\chi$: diamagnetic susceptibility

[a] Determined by ICP method.

respectively. Meanwhile, at lower temperature, a first maximum $\langle T_B\rangle \sim 10$ K for both samples (ZFC observed directly on the curve) can be determined. Thus, the broad energy barrier distribution observed and the presence of more than one maximum are strong evidence of a broad distribution of nanoparticle sizes. In addition, the general behavior of thermal dependences of magnetization confirms the presence of different magnetic phases of iron oxides. Thus, taking into account that the continuous increase of the FC magnetization curves with decreasing temperature indicates that the nanoparticles are non-interacting, it is possible to assume an Arrhenius type relaxation (Eq. (5)), where $\langle T_B\rangle$ corresponds to the blocking of particles of an average volume $\langle V\rangle$, according to:

$$\ln(\tau_m/\tau_o)T_B \cdot k_B = KV \quad (5)$$

T_B: blocking temperature
K: effective anisotropy constant
k_B: Boltzmann's constant,
τ_m: measurement time ($\tau_m \sim 100$ s for SQUID measurements)
τ_o: characteristic time of nanoparticles ($\tau_o \sim 10^{-11}$ to 10^{-9}).

By using this equation and assigning the first maximum ($\langle T_B\rangle \sim 10$ K) of the ZFC curve for the Fe/M(1) sample to iron oxide nanospecies of very small size formed inside the channels (≤ 3.5 nm), the constant anisotropy for this magnetic phase could be calculated as $K = 1.53.10^5$ J/m^3. Then, assuming that the magnetic behavior of the lower loaded sample mainly arises from this superparamagnetic phase (present inside mesochannels as well as onto the external surface), whose constant was already calculated, the size of nanospecies associated with the second maximum of the ZFC curve (79 K) was calculated as 7 nm. In this way, the size of the nanospecies responsible for the superparamagnetic regime at room temperature, which are not detectable by XRD due to their nanometer size, could be determined.

In addition, for the Fe/M(15) sample (Fig. 9B) the first maximum in the ZFC curve is observed at approximately the same temperature as that corresponding to the Fe/M(1) sample, suggesting that both samples have the same magnetic phase inside their channels. Then, the second maximum observed at lower temperature (70 K) would be indicating the lower size of the superparamagnetic particles present on the external surface of this sample with respect to Fe/M(1). This fact is probably a consequence of the growth of magnetically blocked particles on the external surface at the expense of superparamagnetic species.

EPR spectroscopy is a very sensitive method for studying the nature and environment of symmetry of different magnetic ions in metal modified molecular sieves. Furthermore, several magnetic phases such as para- and ferromagnetic nanoparticles and/or nanoclusters with superparamagnetic behavior can be easily detectable by this method [47]. However, antiferromagnetic and

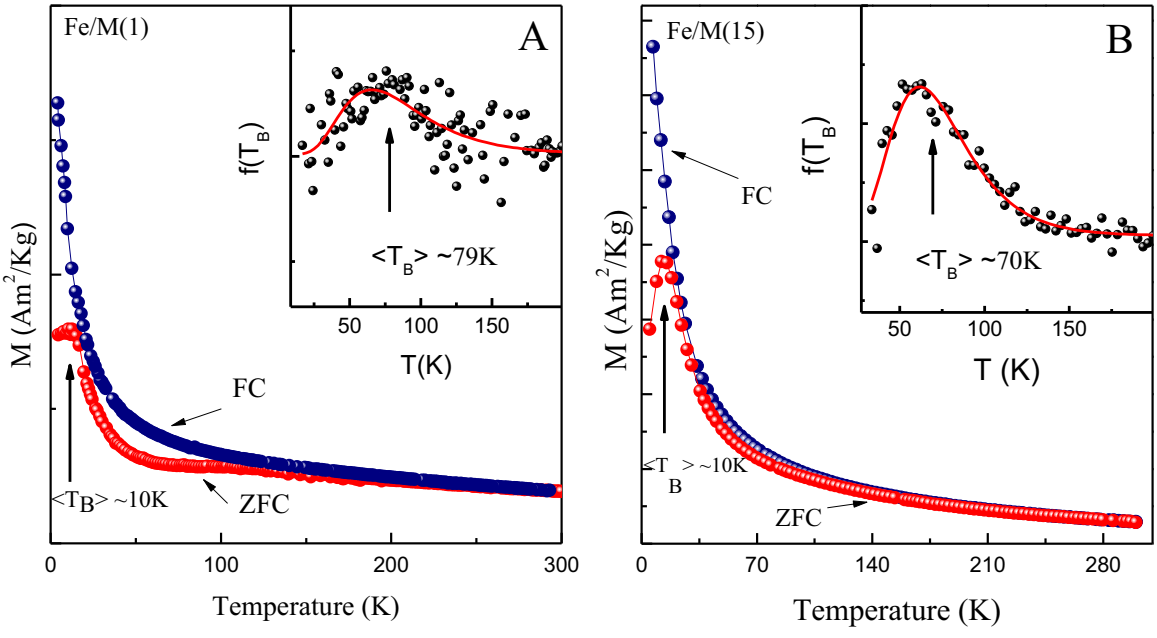

Fig. 9. Magnetization versus temperature measurements following the zero-field-cooling (ZFC) and field-cooling (FC) protocols for samples: Fe/M(1) and Fe/M(15), measured with a 0.01 T applied field.

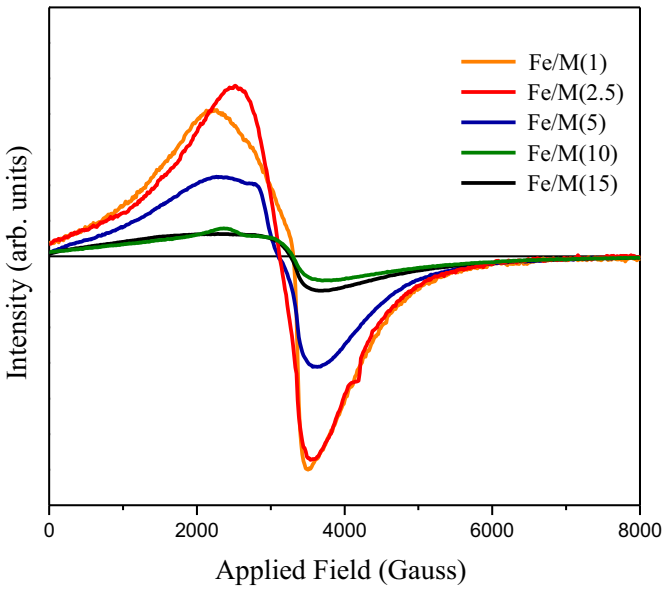

Fig. 10. EPR spectra measured at room temperature for all samples of Fe/M(x) studied.

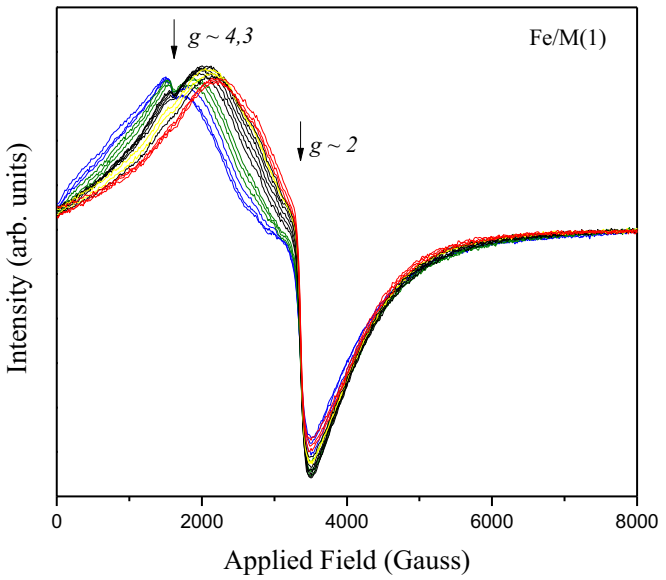

Fig. 11. EPR spectra of Fe/M(1) measured in a temperature range of 123 K (blue, left) to 300 K (red, right). (For interpretation of the references to color in this figure legend, the reader is referred to the web version of this article.)

diamagnetic phases are not detectable by EPR spectroscopy [48]. Therefore, given these considerations, from the EPR spectra, it was possible to infer the nature and symmetry of the iron ions in the samples synthesized in the present work.

In Fig. 10, the EPR spectra of all samples measured at room temperature are shown. Since iron is the only possible source of resonant signal, the intensity of this signal is presented per gram of iron in arbitrary units. Then, the values of gyromagnetic tensor (g) were estimated from the spectra using the following formula [49].

$$g=\frac{h.\,\upsilon}{\beta.\,H_r} \tag{6}$$

H_r: resonance field
υ: frequency used for the measurements ($9.5.10^9\ s^{-1}$)
β: Bohr magneton ($9.27.10^{24}$ J)

For all systems, the spectra show an asymmetric lineshape with a main broad resonance centered on $g\sim2$. This signal may be associated with the strong interaction between iron ions in nanospecies of superparamagnetic iron oxide. Thus, this asymmetric lineshape with a broad linewidth (>1000 G) usually appears in powder samples due to particle sizes with a random distribution of magnetic anisotropy axes in space [50,51]. These results complement magnetization measurements, and support the hypothesis of a broad size distribution of nanospecies. Meanwhile, it can be seen that the area under the curves decreases with increasing metal content. This fact would be indicating that the superparamagnetic signal decreases due to the growth of oxide nanoparticles, which exceed the critical size leaving the superparamagnetic regime to form a magnetically blocked hematite phase. This behavior is consistent with results obtained previously from the magnetization *vs* applied field and FC–ZFC curves.

The evolution with the temperature of the EPR spectra for the Fe/M(1) sample in the range of 123–300 K is shown in Fig. 11. Here, two main signs ($g\sim2$ and $g\sim4.3$) can be assigned to two different species of Fe^{3+}. The first signal ($g\sim2$), already associated with Fe^{3+} ions in the superparamagnetic nanoclusters and/or nanoparticles, becomes progressively more asymmetric with decreasing temperature. This low temperature performance can be attributed to a bimodal size distribution and to the randomly distributed absorption along the axis direction of anisotropy, providing a more asymmetric lineshape with decreasing temperatures [52].

Meanwhile, the signal corresponding to $g\sim4.3$ may be associated with the presence of isolated Fe^{3+} cations linked to O atoms on the surface of the matrix, which were also evidenced by UV–vis DR and XPS spectroscopy [26]. This signal located at $g=4.3$ becomes more remarkable at lower temperatures, confirming its paramagnetic nature. Note that this signal is very weak at room temperature (not observed in Fig. 9) probably because it is masked by the main superparamagnetic signal.

4. Conclusions

Magnetic nanocomposites of iron-modified MCM-41 were successfully synthesized by the wet impregnation method. All samples exhibited Lewis acidity associated with isolated Fe species as well as with iron oxide nanospecies, which for the higher loaded samples are blocking the silanols of the MCM-41 structure. In order to gain further knowledge on the nature of such iron species present on the solids, a synergic analysis by applying different magnetic characterization techniques (M *vs* H, FC–ZFC, EPR) was carried out. All samples showed a main superparamagnetic contribution arising from iron oxide nanoclusters and/or nanoparticles of very small size and finely dispersed on surface. Then, the growth of these Fe oxide species, above the critical size corresponding to superparamagnetic regimen, led to the appearance of a magnetically blocked phase (hematite nanoparticles) on the external surface (observed also by TEM). In this sense, from fitted parameters of magnetization curves, a decrease of μ_{SP} with increasing iron loading allowed us to corroborate the growth in size of the oxide particles at the expense of superparamagnetic clusters/nanoparticles of smaller size. Finally, a bimodal distribution of nanospecies in superparamagnetic regime could be determined from the FC–ZFC curves; the corresponding anisotropy constant for this phase was calculated as $K=1.53.10^5$ J/m^3, and the size of these nanospecies could be estimated.

Acknowledgments

The authors are grateful to Comision Nacional de Investigaciones Cientifico Tecnológicas (CONICET) (1), Universidad Tecnológica Nacional-Facultad Regional Córdoba (UTN-FRC) (2) and Facultad de Matemática Astronomía y Física-Universidad Nacional de Córdoba (FaMAF-UNC) (3) for the financial support. The authors also thank to Ph.D. Silvia Urreta for her valuable contribution in the discussion of results and PhD. Silvia Mendieta for the assistance with SEM micrographs.

References

[1] J. Corchero, A. Villaverde, Biomedical applications of distally controlled magnetic nanoparticles, Trends Biotechnol. 27 (2009) 468–476.
[2] I. Safarik, M. Safarikova, Magnetic nano- and microparticles in biothecnology, Chem. Pap. 63 (2009) 497–505.
[3] A. Figuerola, R. Di Corato, L. Manna, T. Pellegrino, From iron oxide nanoparticles towards advanced iron-based inorganic materials designed for biomedical applications, Pharmacol. Res. 62 (2010) 126–143.
[4] J. Oh, J. Park, Iron oxide-based superparamgnetic polymeric nanomaterials; design, preparation, and biomedial application, Prog. Polym. Sci. 36 (2011) 168–189.
[5] K. Widder, A. Senyei, D. Scarpelli, Magnetic microspheres: a model system for site specific drug delivery in vivo, Proc. Soc. Exp. Biol. Med. 58 (1978) 141–146.
[6] A. Senyei, K. Widder, C. Czerlinski, Magnetic guidance of drug-carrying microspheres, J. Appl. Phys. 49 (1978) 3578–3583.
[7] C. Kresge, M. Leonowicz, W. Roth, J. Vartuli, J. Beck, Ordered mesoporous molecular sieves synthesized by a liquid-crystal template mechanism, Nature 359 (1992) 710–712.
[8] J. Beck, J. Vartuli, W.J. Roth, M. Leonowicz, C. Kresge, K. Schmitt, C.T.W. Chu, D. Olson, E. Sheppard, S. McCullen, J. Higgins, J. Schlenker, A new family of mesoporous molecular sieves prepared with liquid crystal templates, J. Am. Chem. Soc. 114 (1992) 10834–10843.
[9] M. Vallet-Regi, F. Balas, D. Arcos, Mesoporous materials for drug delivery, Angew. Chem. Int. Ed. 46 (2007) 7548–7558.
[10] N. Botterhuis, Q. Sun, P. Magusin, R. Santen, N. Sommerdijk, Hollow silica spheres with an ordered pore structure and their application in controlled release studies, Chem. Eur. J. 12 (2006) 1448–1456.
[11] Q. Pankhurst, J. Connolly, S. Jones, J. Dobson, Applications of magnetic nanoparticles in biomedicine, J. Phys. D: Appl. Phys. 36 (2003) 167–181.
[12] M. Vallet-Regi, Ordered mesoporous materials in the context of drug delivery systems and bone tissue engineering, Chem. Eur. J. 12 (2006) 5934–5943.
[13] Q. Yang, S. Wang, P. Fan, L. Wang, Y. Di, K. Lin, F. Xiao, pH.-Reponsive Carrier System, Based on carboxylic acid modified mesoporous silica and polyelectrolyte for drug delivery, Chem. Mater. 17 (2005) 5999–6003.
[14] S. Giri, B. Trewyn, M. Stellmaker, V. Lin, Stimuli-responsive controlled-release delivery system based on mesoporous silica nanorods capped with magnetic nanoparticles, Angew. Chem. Int. Ed. Engl. 44 (2005) 5038–5044.
[15] K.M. Krishnan, Biomedical nanomagnetics: a spin through possibilities in imaging, diagnostics, and therapy, IEEE Trans. Magn. 46 (2010) 2523–2558.
[16] L. Néel, Théorie du traînage magnétique des ferromagnétiques en grains fins avec application aux terres cuites, Ann. Geophys. 5 (1949) 99–136.
[17] F. Bødker, S. Mørup, Size dependence of the properties of hematite nanoparticles, Europhys. Lett. 52 (2000) 217–223.
[18] A. Debrassi, C. Burger, C. Rodrigues, N. Nedelko, A. Slawska-Waniewska, P. Dluzewski, K. Sobczak, J. Greneche., Synthesis, characterization and in vitro drug release of magnetic N-benzyl-O-carboxymethylchitosan nanoparticles loaded with indomethacin, Acta Biomater. 7 (2011) 3078–3085.
[19] S. Kolotilov, O. Shvets, O. Cador, N. Kasian, V. Pavlov, L. Ouahab, V. Ilyin, V. Pavlishchuk, Synthesis, structure and magnetic properties of porous magnetic composite, based on MCM-41 molecular sieve with Fe_3O_4 nanoparticles, J. Solid State Chem. 179 (2006) 2426–2432.
[20] N. Fellenz, S. Marchetti, J. Bengoa, R. Mercader, S. Stewart, Synthesis and magnetic characterization of magnetite particles embedded in mesoporous MCM-41, J. Magn. Magn. Mater. 306 (2006) 30–34.
[21] I. Ursachi, A. Vasile, A. Ianculescu, E. Vasile, A. Stancu, Ultrasonic-assisted synthesis and magnetic studies of iron oxide/MCM-41 nanocomposite, Mater. Chem. Phys. 130 (2011) 1251–1259.
[22] V. Elías, M. Crivello, E. Herrero, S. Casuscelli, G.A. Eimer, Some considerations to optimize the synthesis procedure and the structural quality of mesostructured silicas, J. Non-Cryst. Solids 355 (2009) 1269–1273.
[23] M. Stearns, Y. Cheng, Determination of para- and ferromagnetic components of magnetization and magnetoresistance of granular Co/Ag films, J. Appl. Phys. 75 (1994) 6894–6898.
[24] A. Patterson, The Scherrer formula for X-Ray particle size determination, Phys. Rev. 56 (1939) 978–982.
[25] H. Klug, L. Alexander, X-ray Diffraction Procedures for Polycrystalline and Amorphous Materials, 2nd ed., John Wiley and Sons, New York, 1974.
[26] N. Cuello, V. Elías, C. Rodriguez Torres, M. Crivello, M. Oliva, G. Eimer, Development of iron modified MCM-41 as promising nano-composites with specific magnetic behavior, Microporous Mesoporous Mater. 203 (2015) 106–115.
[27] C. Chanquía, L. Andrini, J. Fernández, M. Crivello, F. Requejo, E. Herrero, G. Eimer, Speciation of copper in spherical mesoporous silicates: from the Microscale to Angstrom, J. Phys. Chem. C 114 (2010) 12221–12229.
[28] B. Chakraborty, B. Viswanathan, Surface acidity of MCM-41 by in situ IR studies of pyridine adsorption, Catal. Today 49 (1999) 253–260.
[29] M. Hunger, U. Schenk, M. Breuninger, R. Gläser, J. Weitkamp, Characterization of the acid sites in MCM-41-type materials by spectroscopic and catalytic techniques, Microporous Mesoporous Mater. 27 (1999) 261–271.
[30] X. Zhao, G. Lu, A. Whittaker, G. Millar, H. Zhu, Comprehensive study of surface chemistry of MCM-41 using 29Si CP/MAS NMR, FTIR, pyridine-TPD, and TGA, J. Phys. Chem. B 101 (1997) 6525–6531.
[31] T. Conesa, J. Hidalgo, R. Luque, J. Campelo, A. Romero, Influence of the acid–base properties in Si-MCM-41 and B-MCM-41mesoporous materials on the activity and selectivity of e-caprolactamsynthesis, Appl. Catal. A 299 (2006) 224–234.
[32] A. Jentys, K. Kleestorfer, H. Vinek, Concentration of surface hydroxyl groups on MCM-41, Microporous Mesoporous Mater. 27 (1999) 321–328.
[33] G. Eimer, S. Casuscelli, C. Chanquia, V. Elías, M. Crivello, E. Herrero, The influence of Ti-loading on the acid behavior and on the catalytic efficiency of mesoporous Ti-MCM-41 molecular sieves, Catal. Today 133 (2008) 639–646.
[34] D. Trongon, S. Nguyen, V. Hulea, E. Dumitriu, S. Kaliaguine, Mono- and bifunctional MFI, BEA and MCM-41 titanium-molecular sieves. Part 1. Synthesis and characterization, Microporous Mesoporous Mater. 57 (2003) 169–180.
[35] D. Srinivas, R. Srivastava, P. Ratnasamy, Transesterifications over titanosilicate molecular sieves, Catal. Today 96 (2004) 127–133.
[36] L. Cedeño, D. Hernández, T. Klimova, J. Ramírez, Synthesis of Nb-containing mesoporous silica molecular sieves analysis of its potential use in HDS catalysts, Appl. Catal. A 241 (2003) 39–50.
[37] A. Sakthivel, S. Dapurkar, N. Gupta, S. Kulshreshtha, P. Selvam, The influence of aluminium sources on the acidic behavior as well as on the catalytic activity of mesoporous H-AlMCM-41 molecular sieves, Microporous Mesoporous Mater. 65 (2003) 177–187.
[38] L. Chen, L. Noreña, J. Navarrete, J. Wang, Improvement of surface acidity and structural regularity of Zr-modified mesoporous MCM-41, Mater. Chem. Phys. 97 (2–3) (2006) 236.
[39] X. Hao, Y. Zhang, J. Wang, W. Zhou, C. Zhang, S. Liu, A novel approach to prepare MCM-41 supported CuO catalyst with high metal loading and dispersion, Microporous Mesoporous Mater. 88 (2006) 38–47.
[40] F. Gao, Y. Zhang, H. Wan, Y. Kong, X. Wu, L. Dong, B. Li, Y. Chen, The states of vanadium species in V-SBA-15 synthesized under different pH values, Microporous Mesoporous Mater. 110 (2008) 508–516.
[41] Y. Segura, P. Cool, P. Kustroeski, L. Chmielarz, R. Dziembaj, E. Vansant, Characterization of vanadium and titanium oxide supported SBA-15, J. Phys. Chem. B 109 (2005) 12071–12079.
[42] M. Anpo, M. Matsuoka, Y. Shioya, H. Yamashita, E. Gimello, C. Monterra, M. Che, H. Patterson, S. Webber, S. Ouellette, M. Fox, Preparation and characterization of the Cu^+/ZSM-5 catalyst and its reaction with NO under UV irradiation at 275 K. In situ photoluminescence, EPR, and FT-IR investigations, J. Phys. Chem. 98 (1994) 5744–5750.
[43] L. Chmielarz, P. Kustrowski, R. Dziembaj, P. Cool, E. Vansant, Catalytic performance of various mesoporous silicas modified with copper or iron oxides introduced by different ways in the selective reduction of NO by ammonia, Appl. Catal. B 62 (1994) 369–380.
[44] I. Babich, Y. Plyuto, P. Van der Voort, E. Vansant, Thermal transformations of chromium acetylacetonate on silica surface, J. Colloid Interface Sci. 189 (1997) 144–150.
[45] L. Pierella, C. Saux, H. Bertorello, P. Bercoff, P. Botta, J. Rivas, Occluded cobalt species over ZSM-5 matrix: design, preparation, characterization and magnetic behavior, Mater. Res. Bull. 43 (2008) 2026–2035.
[46] D. Dumitriu, R. Barjega, L. Frunza, D. Macovei, T. Hu, Y. Xie, V. Parvulescu, S. Kaliaguine, BiOx clusters occluded in a ZSM-5 matrix: preparation, characterization, and catalytic behavior in liquid-phase oxidation of hydrocarbons, J. Catal. 219 (2003) 337–351.
[47] J. Dormann, D. Fiorani, Magnetic Properties of Fine Particles, Elsevier Science Publishers, 1992.
[48] S. Badamali, A. Sakthivel, P. Selvam, Tertiary butylation of phenol over mesoporous H–FeMCM-41, Catal. Lett. 65 (2000) 153–157.
[49] V. Elías, E. Sabre, E. Winkler, M. Satuf, E. Rodriguez-Castellón, S. Casuscelli, G. Eimer, Chromium and titanium/chromium-containing MCM-41 mesoporous silicates as promising catalysts for the photobleaching of azo dyes in aqueous suspensions. a multitechnique investigation, Microporous Mesoporous Mater. 163 (2012) 185–195.
[50] Ch. P. Poole, Electron Spin Resonance, Second Edition, Dover Publications Inc., 1983.
[51] A. Gervasini, C. Messi, P. Carniti, A. Ponti, N. Ravasio, F. Zaccheria, Insight into the properties of Fe oxide present in high concentrations on mesoporous sílica, J. Catal. 262 (2009) 224–234.
[52] A. Jahagirdar, N. Dhananjaya, D. Monika, C. Kesavulu, H. Nagabhushana, S. Sharma, B. Nagabhushana, C. Shivakumara, J. Rao, R. Chakradhar Spectrochimica, Structural, EPR, optical and magnetic properties of a-Fe_2O_3 nanoparticles, Spectrochim. Acta A 104 (2013) 512–518.